

Breaking waves and near-surface sea spray aerosol dependence on changing winds: Wave breaking efficiency and bubble-related air-sea interaction processes

P A Hwang, I B Savelyev and M D Anguelova

Naval Research Laboratory, 4555 Overlook Ave SW, Washington DC 20375 USA

E-mail: paul.hwang@nrl.navy.mil

Abstract. Simultaneous measurements of sea spray aerosol (SSA), wind, wave, and microwave brightness temperature are obtained in the open ocean on-board Floating Instrument Platform (FLIP). These data are analysed to clarify the ocean surface processes important to SSA production. Parameters are formulated to represent surface processes with characteristic length scales spanning a broad range. The investigation reveals distinct differences of the SSA properties in rising winds and falling winds, with higher SSA volume in falling winds. Also, in closely related measurements of whitecap coverage, higher whitecap fraction as a function of wind speed is found in falling winds than in rising winds or in older seas than in younger seas. Similar trend is found in the short scale roughness reflected in the microwave brightness temperature data. In the research of length and velocity scales of breaking waves, it has been observed that the length scale of wave breaking is shorter in mixed seas than in wind seas. For example, source function analysis of short surface waves shows that the characteristic length scale of the dissipation function shifts toward higher wavenumber (shorter wavelength) in mixed seas than in wind seas. Similarly, results from feature tracking or Doppler analysis of microwave radar sea spikes, which are closely associated with breaking waves, show that the magnitude of the average breaking wave velocity is smaller in mixed seas than in wind seas. Furthermore, breaking waves are observed to possess geometric similarity. Applying the results of breaking wave analyses to the SSA and whitecap observations described above, it is suggestive that larger air cavities resulting from the longer breakers are entrained in rising high winds. The larger air cavities escape rapidly due to buoyancy before they can be fully broken down into small bubbles for the subsequent SSA production or whitecap manifestation. In contrast, in falling winds (with mixed seas more likely), the shorter breaker entrains smaller and more numerous air cavities that stay underwater longer for more efficient bubble breakup by turbulence and prolonging the surface disturbances attributable to wave breaking. For low winds, the breaking scale is small and with high efficiency for SSA or whitecap generation; the trend of rising or falling wind is less important.

1. Introduction

Breaking of ocean surface waves plays an important role in many air-sea interaction processes. For example, it is a main source of turbulence on the upper ocean layer; breaking waves entrain bubbles and enhance air-sea gas exchange; returning to the ocean surface, the entrained air bubbles appear as whitecaps enhancing the surface albedo and modifying heat and gas transfer; the returning bubbles also cause surface disturbances and contribute to the breaking-wave-induced surface roughness; the formation of bubbles detached from the entrained air cavity is the main source of underwater ambient



noise; and bursting of bubbles at the sea surface is one of the main generation sources of sea spray aerosols, which represent an important member of the atmospheric aerosol population.

In this paper, we report results of a field experiment addressing the effect of wave breaking on SSA production. Simultaneous measurements of SSA, wind, wave and microwave brightness temperature are obtained in the open ocean on-board FLIP in the Pacific Ocean about 200 km off the California coast [1]. Over a period of about two weeks of free drifting, the experiment encountered a wide range of environmental conditions with wind speed U_{10} ranging between 1.9 and 15.6 m/s, and significant wave height H_s between 1.0 and 4.5 m. Based on the field notes, there was no rain event during the period reported in this paper. Here we focus on results showing distinctly higher SSA properties (number, volume, flux) in a falling wind event than that in a rising wind event (for the same wind speed). Similar results have been reported in Ovadnevaite *et al.* [2] and in the closely related whitecap observations of Callaghan *et al.* [3], though the physical reasons behind these observations are not clear.

In previous investigations of the length and velocity scales of breaking waves [4–8], it is found that the breaking wavelength (velocity) scale is shorter (slower) in mixed seas compared to that in wind seas. From the consideration of breaking wave geometric similarity [9], the size of the breaking patches and the air cavities entrained into water is proportional to the breaking wavelength. Due to the buoyancy effect, the large cavities escape soon after breaking entrainment. As a result, the shorter dwell time of the entrained large air cavity decreases the effective air volume useful for subsequent bubble cloud generation and other related processes. Thus, it is deduced that larger breaking is less efficient in bubble-related processes such as production of SSA or whitecaps. Considering that mixed seas are more likely to occur in falling wind events and wind seas in rising winds, we propose that the efficiency of wave breaking is the cause of the observed differences in the SSA generation or whitecap manifestation between rising and falling wind conditions. In other words, the breaking efficiency in these bubble-related processes is influenced by the breaking length scale through the entrained air cavity size, leading to the observed higher SSA or whitecaps in falling winds than in rising winds.

In the following, we present the analysis of the field measurements in section 2; the interpretation of the SSA differences in rising and falling winds is discussed in section 3 and a summary is given in section 4.

2. Analysis

The measured wind, wave and microwave brightness temperature are analyzed to formulate parameters that represent surface processes with distinctively different characteristic length scales ranging from a few centimeters to a few decameters. The short scale is represented by the roughness component of 10.7-GHz microwave brightness temperature ΔT_b . This quantity is derived from the difference between the horizontal and vertical polarizations of the wind-induced deviation of the brightness temperature from the flat surface values: $\Delta T_b = \delta T_{bH} - \delta T_{bV}$. Using the method described in Hwang [10], the wind-induced deviations δT_{bH} and δT_{bV} can be separated into the roughness and foam components, a brief summary is given in Appendix A. Because the foam components of δT_{bH} and δT_{bV} are small for the wind conditions in our experiment, they almost cancel each other out, leaving ΔT_b to be contributed predominantly by the centimeter scale surface roughness to the 10.7 GHz-emission.

The long-scale process is represented by the surface wave energy dissipation rate E_r . The wave energy dissipation rate is calculated from the energy conservation equation governing the wind-generated waves and coupled with the fetch- or duration-limited wind wave growth functions [11]. Expressed as a dimensionless function, it is given by $\frac{E_r}{\rho_a U_{10}^3} = 0.20 \omega_*^{3.3} \eta_*$, where ρ_a is the density of air (1.2 kg/m³), $\omega_* = \omega_p U_{10}/g$ and $\eta_* = \eta_{rms}^2 g^2 / U_{10}^4$ are dimensionless wave spectral peak frequency ω_p and wave variance η_{rms}^2 , respectively, U_{10} is the neutral wind speed at 10-m elevation, and g is the gravitational acceleration. In mixed seas, it is necessary to separate the swell and wind sea components in order to make use of the energy dissipation rate equation derived from the wind wave growth

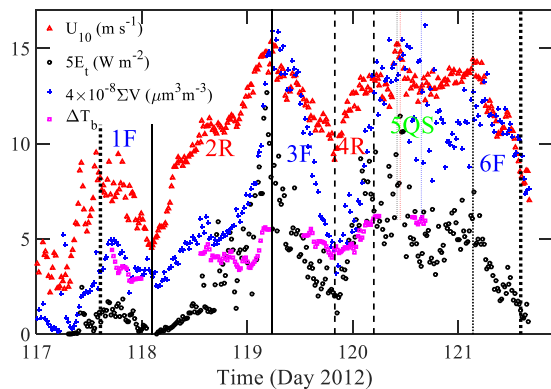


Figure 1. Time series of U_{10} , E_t , ΔT_b and ΣV , with six episodes (rising, falling, quasi-steady) identified.

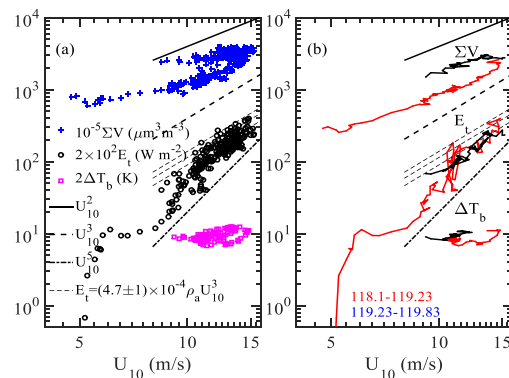


Figure 2. Power-law dependency of ΣV , E_t , and ΔT_b on U_{10} : (a) Data unsorted; and (b) 2 consecutive time segments of rising (red) and falling (black) wind events.

functions. The procedure of swell–sea separation described in Hwang *et al.* [12] is used in this study. Further detail is given in Appendix B.

Figure 1 shows the time series of wind speed U_{10} , energy dissipation rate E_t , brightness temperature deviation ΔT_b , and SSA volume ΣV , which represents the total atmospheric loading of aerosols with ambient radius ranging between 1 and 25 μm . The time series clearly illustrates the fluctuating feature of the events. ΣV , E_t , and ΔT_b show quadratic to cubic power-law dependence on wind speed for moderate to higher winds (figure 2a). For reference, U_{10}^2 , U_{10}^3 and U_{10}^5 line segments are superimposed; they also serve as partitions separating various measurements. We are especially interested in the E_t parameter in this paper; also plotted are the set of empirical relations $E_t = (4.7 \pm 1) \times 10^{-4} \rho_a U_{10}^3$ derived from examining the surface wave dissipation rates in several field datasets [11, 13]. The E_t dependence on wind speed in the present dataset is also close to cubic in higher winds.

A closer inspection reveals that the data are constituted of two main populations following similar wind speed dependence but with different absolute magnitudes. In figure 2b, the temporal evolutions of ΣV , E_t and ΔT_b in two consecutive time segments of rising and falling winds are highlighted by different colors (2R and 3F marked by vertical line segments in figure 1). Comparing the two events, a “hysteresis” in $\Sigma V(U_{10})$ is obvious. Figure 3 shows $\Sigma V(U_{10})$, $\Sigma V(E_t)$ and $E_t(U_{10})$ of all six events: three rising winds in black, two falling winds in cyan and one quasi-steady wind in green. The rising and falling wind events aggregate in separate clusters, and are the focus of this paper.

Because of the low settling velocity of aerosols, a tempting interpretation of the observed hysteresis is that once aerosols are suspended in rising winds, they stay aloft during a falling wind period thus resulting in higher number for a given wind speed in falling winds than in rising winds. However, a similar response lag is found in the roughness component of brightness temperature (figure 2b); the centimeter scale short surface waves contributing to the surface roughness certainly do not have the long dwell time of aerosol particles.

The contrast between falling and rising winds is conspicuously mixed in the wind sea energy dissipation rate in comparison to the SSA and ΔT_b observations. In the high wind region in particular, the energy dissipation rate is generally less in falling winds than in rising winds for the same wind speed. This is reasonable considering that rising winds carry additional forcing of wind speed acceleration. But then why the reverse trend in SSA flux and surface roughness? As noted in the last paragraph, although it is tempting to interpret the SSA observation of the hysteresis as due to the long dwell time of small aerosols once suspended in air, this argument cannot be applied to the short scale roughness as well as the whitecap observations, of which the constituent bubble lifetime is measured in seconds. A more plausible interpretation applicable to all three observations (SSA, whitecaps,

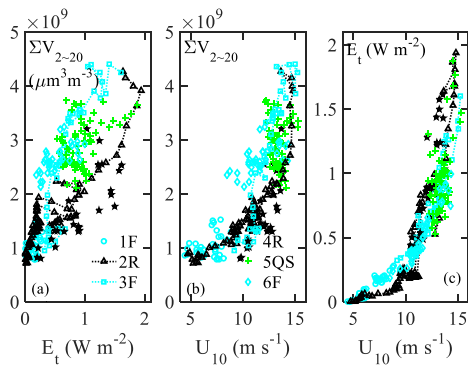


Figure 3. ΣV as a function of (a) E_t , and (b) U_{10} ; and (c) $E_t(U_{10})$; rising winds (black), falling winds (cyan) and quasi-steady (green).

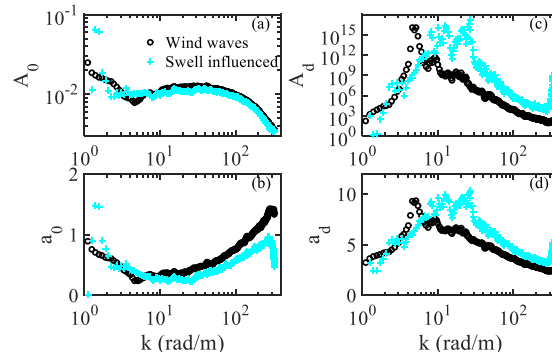


Figure 4. (a) A_0 , and (b) a_0 of the roughness spectrum; (c) A_d , and (d) a_d of the dissipation function. Reproduced from [6]

brightness temperature deviation) is needed. This will be explored further with help from previous investigations of the length and velocity scales of breaking waves (section 3).

3. Discussion

In the research of length and velocity scales of breaking waves, field measurements show that the length scale of wave breaking is shorter in mixed seas than in wind seas. For example, following the analysis of source function balance described in Phillips [14], Hwang and Wang [6] present field data of short surface wave spectra obtained by a free-drifting wave gauge system. Experimental results led to the establishment of a similarity relation of the short wave spectral component: $B(u_* / c; k) = A_0(k)(u_* / c)^{a_0(k)}$, from which a general spectral dissipation function was formulated [14]: $f_d(B) = A_d(k)B^{a_d(k)}$. Sorting the field data into wind sea and mixed sea groups, the analysis shows that the characteristic length scale of the dissipation function shifts toward higher wavenumber (shorter wavelength) in mixed seas compared to that in wind seas, as illustrated in the upshift of the characteristic wavenumber of f_d from wind sea (black) to mixed sea (cyan) in figures 4c and 4d. Similarly, based on feature tracking [5] or Doppler analysis [7, 8] of microwave radar sea spikes, which are closely associated with breaking waves, the average breaking wave velocity is smaller with swell presence compared to that in pure wind seas (figure 5).

Here we clarify that the characteristic breaking length scale discussed in Hwang and Wang [6] is derived from the observations of wave spectral function variations with respect to the wind forcing parameter u_* / c . It therefore refers to the scale of waves that break, and not the length scale over which the wave energy dissipates. This distinction also applies to the observations of breaking velocities using feature tracking and Doppler analysis of sea spikes.

Applying the result of wave breaking analyses to the SSA, microwave brightness temperature and whitecap observations described in section 2, and coupled with the geometric similarities relating the breaking wavelength and breaking wave patch as well as the vertical and horizontal scales of breaking patches [9] as illustrated in figure 6, it is suggestive that larger air cavities resulting from the longer breakers are entrained in rising high winds. The larger air cavities escape rapidly due to buoyancy before they can be fully broken down into small bubbles for the subsequent SSA production or whitecap manifestation. In contrast, in falling winds (with mixed seas more likely), the shorter breaker entrains smaller and more numerous air cavities that stay underwater longer for more efficient bubble breakup by turbulence as well as prolonging the surface disturbance induced by wave breaking. For low winds, the breaking scale is small, also resulting in high efficiency of SSA or whitecap generation, and the trend of rising or falling in low winds is less distinguishable.

Based on our multisensor measurements, the E_t threshold of breaking efficiency transition in rising and falling winds is estimated to be 0.35 W/m^2 (figure 3a). As shown in figure 3b, the magnitude and

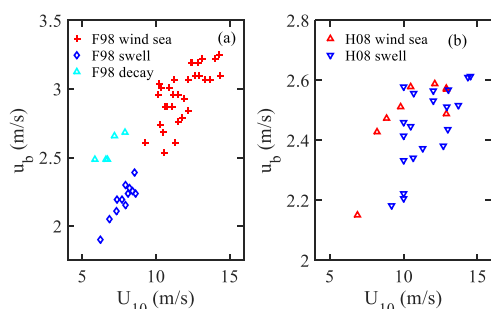


Figure 5. The breaking velocity deduced from (a) feature tracking [5] and (b) Doppler processing [7-8] of radar sea spikes. The breaking velocity is smaller in mixed seas (blue) in comparison to the value in wind seas (red). Adapted from figure 9 of Hwang *et al.* [7].

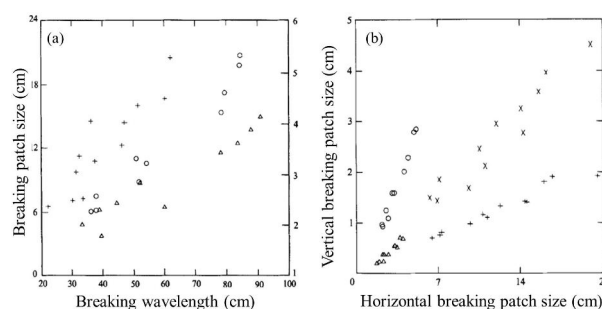


Figure 6. Laboratory results showing geometric similarity relating (a) the breaking wavelength and breaking patch size, and (b) the vertical and horizontal scales of breaking patches; different symbols represent different analyses. Adapted from figures 15 and 16 of Hwang *et al.* [9].

the rate of change of the SSA volume are considerably higher in falling winds (light symbols) than in rising winds (dark symbols). In comparison, the computed energy dissipation rate (figure 3c) shows mixed results: for high winds ($> \sim 10$ m/s), the dissipation rate is slightly higher in rising winds than in falling winds; for low wind speeds ($< \sim 10$ m/s) the trend is reversed. The higher rate of change represented by the slope of $\Sigma V(E_i)$ may be interpreted as a higher efficiency of breaking production in low or falling winds (figure 3a).

For a more comprehensive treatment, other physical aspects need to be considered. Examples include variation in wave growth rate in response to the nonstationarity of accelerating winds leading to an imbalance between dissipation and wind input in rising winds, and a potential relaxation of sea state towards equilibrium in falling winds leading to greater than average wave energy dissipation, essentially the opposite effect as in rising winds. Also, the relative size of air cavities entrained during falling and rising seas may be related to the spilling vs. plunging breakers. Photographic evidence suggests that plungers initially entrain larger air cavities than spillers [15]. Furthermore, it is necessary to investigate the timescales of air cavities escaping from underwater compared to the fragmentation time under turbulence [16]. These subjects, while interesting, cannot be addressed adequately due to space limitations.

As a final note, it is likely that the signature in the aerosol size spectra may be very similar between the dwell time consideration and the breaking efficiency consideration through the sizes of the breaking patches and entrained cavities. It is easy to deduce that if smaller particles are more abundant in falling winds than in rising winds, it could be evidence that particle residence time is responsible for increased concentrations during fallings winds. However, a more efficient breakup of the entrained air cavity also leads to the resulting bubble cloud shifting its population to smaller sizes, and the subsequent enhancement of small aerosols [17, 18].

Figure 7a shows four SSA volume spectra, each the average over 2 consecutive hours of measurements. These four spectra are selected, two each, in rising- and falling-wind periods. The average wind speeds are all within 11.0 ± 0.1 m/s with standard deviations between 0.2 and 0.8 m/s. In general, the size range is broader in falling winds than in rising winds, consistent with our expectation from more efficient breakup of the entrained bubble cavities, but the increased small size population can also be from longer dwell time as discussed in the last paragraph. Figure 7b shows the SSA flux spectra and the comparison with three models [17, 18, 19]. The size distribution in our field data is close to exponential: $dF/d\ln r \sim \exp(-ar)$. For $r_{80} < \sim 10$ μm , the results are in best agreement, in both magnitude and size distribution, with the Monahan *et al.* bubble-based model [17], which may reflect the breaking efficiency mechanism of bubble-related processes as described in this paper. In summary, the breaking efficiency consideration provides a consistent explanation of the behavior of aerosols,

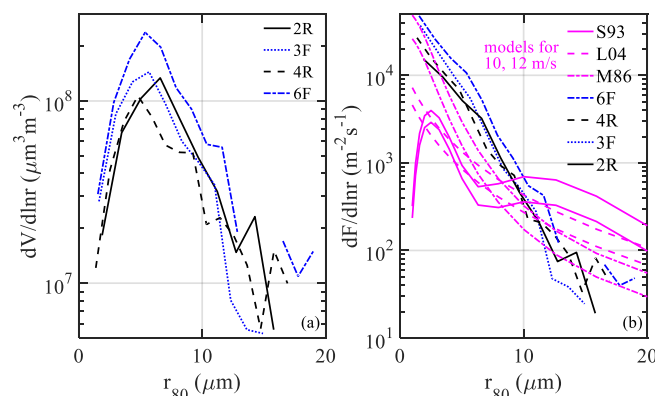


Figure 7. Four size spectra in rising and falling winds. The respective time period, mean RH and mean with standard deviation of U_{10} are [118.56~118.65, 119.64~119.73, 119.86~119.95, 121.45~121.53 d], [71.4, 81.7, 89.3, 84.6 %] and [10.9 ± 0.4 , 11.1 ± 0.2 , 11.0 ± 0.8 , 10.9 ± 0.5 m/s] for [2R, 3F, 4R, 6F]: (a) volume spectra, and (b) flux spectra, also shown are computed results for $U_{10} = 10$ and 12 m/s of three models [17, 18, 19], labelled respectively M86, L04 and S93.

whitecaps and brightness temperature in rising winds and falling winds. In comparison, the convenient argument of residence time can only be applied to the aerosol data but not the observations of whitecaps and brightness temperature.

For a more definitive analysis, it is necessary to have independent observations of the wave breaking properties, such as the entrained cavity size, depth of entrainment, the resulting bubble cloud size spectrum, and the turbulence properties. Our experiment does not have the necessary independent breaking observations for a definitive proof, so indirect evidence from previous relevant experiments and wave breaking analyses has been used. We hope that future observations can provide more direct measurements to support or refute the suggested hypothesis of wave breaking efficiency on bubble-related processes.

4. Summary

Several studies have shown distinct differences in the length and velocity scales of breaking waves in wind seas and mixed seas. It is deduced that the different breaking scales produce different sizes of breaking patches and air cavities entrained during the breaking process. This size difference may be the root cause of the observed higher SSA flux, whitecap coverage and surface roughness reflected in microwave brightness measurements in falling winds than those in rising winds.

Acknowledgments. This work is sponsored by the Office of Naval Research (NRL program elements 61153N). NRL publication number: NRL/PP/7260-15-0135. We are grateful for the comments and suggestions from an anonymous reviewer.

Appendix A: Foam and roughness components of microwave brightness temperature

There are two main components of the wind-induced deviation of the brightness temperature T_b from the flat surface value: foam and roughness. The formula connecting T_b and the sea surface temperature T_s can be written as [10]

$$T_{bp} = (e_{0p} + \delta e_{fp} + \delta e_{rp}) T_s, \quad (\text{A1})$$

where subscript p is polarization, e_0 is the emissivity of the flat surface without foam, δe_f is the emissivity correction due to foam for the flat surface contribution, and δe_r is the rough surface contribution. These three components are given by:

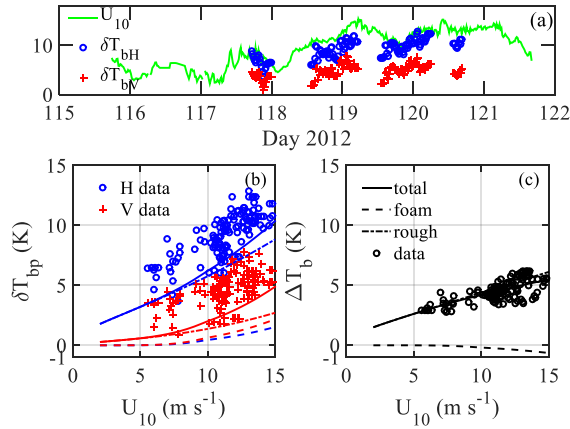


Figure A1. Processed results of the brightness temperature T_b measurements: (a) U_{10} , T_b and δT_{bp} . (c) $\Delta T_b = \delta T_{bH} - \delta T_{bV}$.

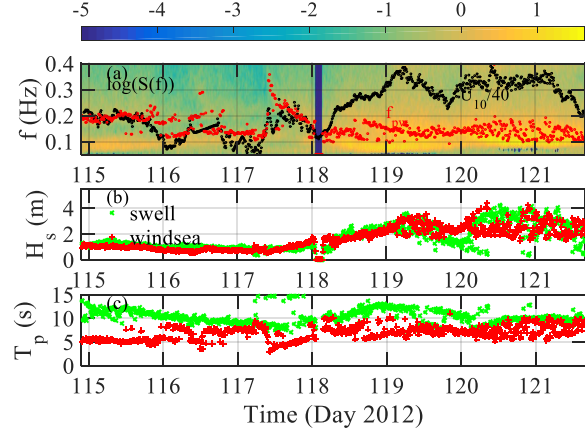


Figure B1. Sea state, swell and wind sea separation: (a) wave spectrum; (b) H_{sw} and H_{ss} ; and (c) T_{pw} and T_{ps} .

$$e_{0p} = 1 - \left| R_{pp}^{(0)} \right|^2, \quad (\text{A2})$$

where $R_{pp}^{(0)}(\varepsilon, \theta)$ is the Fresnel reflection coefficient of polarization p ; the value is determined by the incidence angle θ and the frequency-dependent relative permittivity ε ,

$$\delta e_{jp} = e_{ep} - e_{0p}, \quad (\text{A3})$$

where e_{ep} is the effective emissivity of the flat surface with foam, and

$$\delta e_{rp} = \int_0^{\infty} \int_{-\pi}^{\pi} W(k', \phi') g_p(f, \theta, \phi, \varepsilon_e, k', \phi') k' d\phi' dk', \quad (\text{A4})$$

where W is the directional ocean surface roughness spectrum with k the surface wave number and ϕ the propagation direction, and g_p is the electromagnetic “weighting” function for the p polarization [20, 21].

The relative permittivity of air and water differ considerably for microwave frequencies, therefore even a small amount of air can produce non-trivial changes in the relative permittivity of the resulting mixture. To account for the effect of entrained air, ideally we need to know the fraction of air in water (void fraction) and the vertical distribution of the bubble clouds carrying the air into water. Considering the lack of detailed information about the bubble cloud distribution and the small penetration depth of microwaves, for example, the skin depth is about 2 mm at 10 GHz [22], Hwang [10] uses the fraction of whitecap coverage as a proxy of the void fraction in the mixing rule for the evaluation of the effective relative permittivity ε_e . The approach renders the emission problem of foam-covered ocean surface to two-dimensional (horizontal). The whitecap fraction represents an upper bound of the void fraction because it is equivalent to assuming 100% of air in the depth of microwave influence under the foamy area, whereas the air entrainment decreases exponentially with water depth [23, 24]. The effective relative permittivity ε_e of the air-water mixture is computed with the quadratic mixing rule in a similar approach as that described in Anguelova [25]:

$$\varepsilon_e = \left[f_a \varepsilon_a^{1/2} + (1 - f_a) \varepsilon_{sw}^{1/2} \right]^2, \quad (\text{A5})$$

where ε_{sw} is relative permittivity of sea water without whitecaps and $\varepsilon_a = 1$ is relative permittivity of air, and f_a is air fraction approximated by the whitecap fraction.

Based on this “equivalent medium” approach, the calculated results are in very good agreement with a global dataset of WindSat microwave radiometer measurements with wind speed coverage up to about 42 m/s [26]. The WindSat includes five microwave frequencies (6, 10, 18, 23 and 37 GHz) for both vertical and horizontal polarizations; see figure 3 in [10], figure 9 in [27] and figure 5 in [28]. The agreement between the model and present measurements is also very good (figure A1).

Appendix B. Wind wave energy dissipation

To emphasize the relevance to wave breaking, the combination of wind and wave data are represented by the wind sea energy dissipation rate [11, 13]. The separation of wind sea and swell components is based on the spectrum integration method [12]. The result of applying the method to the FLIP data is shown in figure B1: (a) displays the time-frequency spectral plot; (b) the significant wave heights of the wind sea and swell components; and (c) the peak wave periods of the wind sea and swell components. There is a gap (the dark band in the spectral plot of figure B1a) in the wave data between $t = 118.043$ and 118.143 d when the pressure sensor depth is adjusted from 3 m to 4 m to prevent breaching. Another adjustment to 5 m is done near $t = 119$ d without stopping data recording. The time series of wind speed and wind sea peak frequency f_{pw} obtained from swell sea separation are superimposed on the wave spectrum plot (figure B1a) to show the complex evolution of the surface wave spectrum in response to fluctuating wind forcing.

The wind sea component of the wave spectrum is used to estimate the spectrally integrated energy dissipation rate attributed to wave breaking [11]:

$$E_t = \alpha \rho_a U_{10}^3, \text{ with } \alpha = 0.20 \omega_{\#}^{3.3} \eta_{\#}. \quad (\text{B1})$$

References

- [1] Savelyev I B *et al* 2014 *Atmos. Chem. Phys.* **14** 11611
- [2] Ovadnevaite J *et al* 2012 *J. Geophys. Res.* **117** D16201.
- [3] Callaghan A *et al* 2008 *Geophys. Res. Lett.* **35** L23609.
- [4] Liu Y *et al* 1998 *IEEE Trans. Antennas Propag.* **46** 27
- [5] Frasier S J *et al* 1998 *J. Geophys. Res.* **103** 18745
- [6] Hwang P A and Wang D W 2004 *Geophys. Res. Lett.* **31** L15301
- [7] Hwang P A *et al* 2008 *J. Geophys. Res.* **113** C02003
- [8] Hwang P A *et al* 2008 *J. Geophys. Res.* **113** C09017
- [9] Hwang P A *et al* 1989 *J. Fluid Mech.* **202** 177
- [10] Hwang P A 2012 *IEEE Trans. Geos. Rem. Sens.* **50** 2978
- [11] Hwang P A and Sletten M A 2008 *J. Geophys. Res.* **113** C02012 (Corrigendum **114** C02015)
- [12] Hwang P A *et al* 2012 *J. Atmos. Oceanic Tech.* **29** 116
- [13] Hwang P A 2009 *J. Geophys. Res.* **114** C11011
- [14] Phillips O M 1984 *J. Phys. Oceanogr.* **14** 1425
- [15] Rapp R J and Melville W K 1990 *Phil. Trans. R. Soc. Lond.* **A331** 735
- [16] Eastwood C D *et al* 2004 *J. Fluid Mech.* **502** 309
- [17] Monahan E C *et al* 1986 *Oceanic Whitecaps and Their Role in Air-sea Exchange Processes* eds Monahan E C and MacNiocaill G (Springer)
- [18] Lewis E R and Schwartz S E 2004 *Sea Salt Aerosol Production: Mechanisms, Methods, Measurements, and Models – A Critical Review* (Washington DC: American Geophysical Union)
- [19] Smith M H *et al* 1993 *Q. J. R. Meteorol. Soc.* **119** 809
- [20] Johnson J T and Zhang M 1999 *IEEE Trans. Geos. Remote Sens.* **37** 2305
- [21] Yueh S H *et al* 1994 *Radio Sci.* **29** 799
- [22] Plant W J 1990 *Surface Waves and Fluxes, Vol. II – Remote Sensing* eds Geernaert G L and Plant W L (Kluwer Academic)
- [23] Wu J 1981 *J. Geophys. Res.* **86** 457

- [24] Hwang P A *et al* 1990 *J. Phys. Oceanogr.* **20** 19
- [25] Anguelova M D 2008 *J. Geophys. Res.* **113** C08001
- [26] Meissner T and Wentz F J 2004 *IEEE Trans. Geosci. Remote Sens.* **42** 1836
- [27] Hwang P A *et al* 2013 *J. Atmos. Oceanic Tech.* **30** 2168
- [28] Hwang P A and Fois F 2015 *J. Geophys. Res.* **120** 3640